The seismic physical modelling laboratory as a tool for design and appraisal of FWI methods

Sergio Romahn and Kris Innanen

ABSTRACT

We applied full waveform inversion of PP seismic data recorded through the CREWES seismic physical modelling laboratory facility. Although physical modelling introduces certain challenges that must be addressed, it represents a potentially unique way of validating and appraising complex methods involving real measurements of seismic waveforms. One key advantage is that we know the subsurface model that we want to solve; therefore, we can monitor model errors almost exactly. Another advantage is that we can control and vary many acquisition parameters. In several respects, we deal with physical modelling data in a similar way we do with real seismic surface data. For example, the wavelet has to be estimated and we must take noise, attenuation, amplitude variations from shot to shot, etc., into account. However, physical modelling data have particularities that need to be addressed, such as source-receiver directivity and changing waveform with offset. We present an early stage, robust workflow for preparation of raw physical modelling data to use as input to FWI; ultimately this will make the CREWES physical modelling lab an almost unique tool for validating and appraising FWI. We show in detail all processing required to make physical modelling data suitable for being inverted. As an important example of practical FWI algorithm, we used iterative modelling, migration and inversion (IMMI) which aims to incorporate standard processing techniques into the full waveform inversion process. This involves several approximations and internal calibration steps. The gradient is approximated for applying on pre-critical reflections using the phase shift plus interpolation (PSPI) migration. We derived non-stationary matched filters from well information to calibrate the gradient. We also iteratively applied Gaussian smoothers to frequency-band fixed migrated data residuals as an alternative form of the frequency multi-scale FWI. The overall recovery of P-wave velocity variations is quite dramatic, though comparison of blind and calibration well information shows that FWI must work hard in order to generate long-wavelength updates that differ significantly from the geology near the calibration wells.

INTRODUCTION

FWI and IMMI

The purpose of FWI is the construction of the actual distribution of Earth properties in the subsurface. The theory of FWI was given by Lailly (1983) and Tarantola (1984). Ever since, many people have contributed to the evolution and development of this technique (Virieux and Operto, 2009). Equation 1 shows the objective function (the sum of squares of the difference between recorded data Ψ and the modelled data Ψ_k at the kth iteration) that is minimized in the FWI scheme.

$$\phi_k = \sum_{s,r} (\Psi - \Psi_k)^2 \tag{1}$$

The gradient of the objective function with respect to the model parameter is equivalent to a depth reverse time migration (RTM) of the data residuals. This gradient points to the direction of minimization of the objective function, but needs to be scaled in order to be converted into a velocity perturbation or velocity update. This is illustrated in Equation 2, in what Margrave et al. (2010) called the fundamental theorem of FWI.

$$\delta v(x,z) = \lambda \nabla_v \phi_k(x,z,w) = \lambda \int \sum_{s,r} \omega^2 \hat{\Psi}_s(x,z,\omega) \delta \hat{\Psi}^*_{r(s),k}(x,z,\omega) d\omega \qquad (2)$$

Where $\delta v(x,z)$ is the velocity update, λ is a scalar constant, ∇_v is the gradient with respect to the velocity model v, $\phi_k(x,z,w)$ is the objective function, w is angular frequency, $\hat{\Psi}_s(x,z,\omega)$ is a model of the source wavefield for source s propagated to all (x,z), $\delta \hat{\Psi}^*_{r(s),k}(x,z,\omega) d\omega$ is the kth data residual for source s back propagated to all (x,z), $*$ means complex conjugation. The residual $\delta \hat{\Psi}^*_{r(s),k}(x,z,\omega)$ is the difference between observed data Ψ_r and modeled data $\Psi_{r,k}$.

IMMI, introduced by Margrave et al. (2012), makes reference to the cycle of FWI. It was thought as an alternative to accomplish FWI by using tools already available in the industry. It aims to facilitate the application of FWI by saving computational time in two of the main steps of the process: the calculation and the scaling of the gradient. Standard FWI uses a two-way wave operator to calculate the gradient, which is time and memory consuming because it propagates both the source and receiver wave fields and makes the snapshots available to apply the correlation imaging condition. The scalar is commonly estimated by line search, which requires more extra forward modellings. More complex methods use an exact or approximate inverse Hessian matrix that is computationally expensive. Romahn and Innanen (2017) showed with synthetic examples that it is possible to obtain the gradient by applying PSPI migration. They also showed that the gradient can be properly scaled by using velocity information from wells. This technique is called well calibration and its computational cost is negligible. The calibration process was described by Margrave et al. (2010). In this work we use a well calibration technique that considers vertical variation in velocity (Romahn and Innanen, 2017).

Physical modelling and FWI

Physical modelling brings the opportunity to test new seismic processing and interpretation techniques outside the synthetic environment, with the advantage of knowing the subsurface model and a total control of acquisition parameters. We put special emphasis on the conditioning of physical modelling data in order to be used as real seismic data. We considered that directivity and waveform-change issues must be addressed before evaluating algorithms intended for real seismic data.

Pratt (1999) used tomographic seismic data from a physical model to validate his waveform-inversion approach in the frequency domain. The author did not consider directivity or waveform-change effects; however, he was able to obtain good results. The fact that he simulated sources and receivers located in wells, may have caused a mitigation of

the transducer effects. Amplitude discrepancies among observed and modelled data were addressed by applying Q compensation.

Another example of physical modelling and FWI was presented by Cai and Zhang (2015) in the workshop Depth Model Building: Full-waveform Inversion, Beijing, China. The work was focused in the differences in phase, amplitude and AVO effects between recorded and synthetic shots, and their impact on FWI. The author did not take into account directivity and waveform change effects of transducers, which may have an impact on their results.

PHYSICAL MODELLING DATA

We simulated a 2D marine survey at the CREWES seismic physical modelling laboratory facility (figure 1-A). The main characteristics of the laboratory, described in Wong et al. (2009), are: a precise six-axes positioning system using linear electric motors and arrays of small ultrasonic source and detector transducers (figure 1-B), improved circuits for driving source transducers, amplifying detected signals and signal digitization, and motor control and digital data acquisition. We used materials such as PVC and acrylic (PLX) to build the model (figure 1-C).
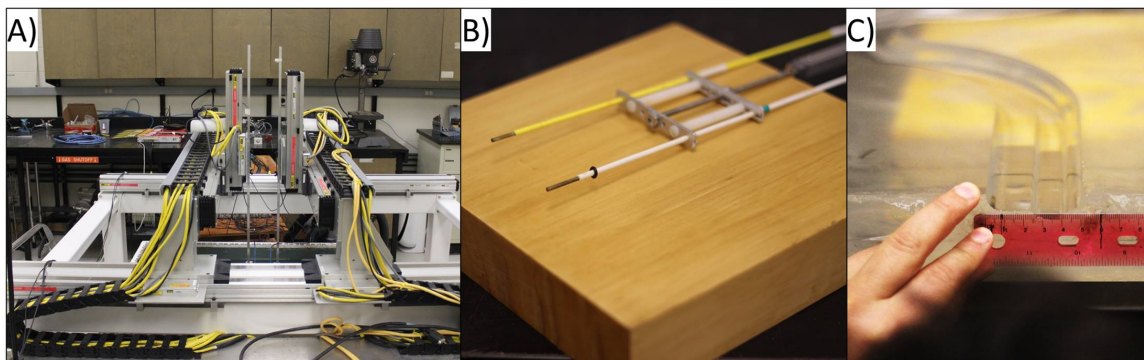

FIG. 1. A) CREWES physical modelling laboratory facility. B) Source and receiver transducer with diameter of 1.3 mm. C) Acrylic slab with a cut channel. Photographs courtesy of Kevin Bertram.

The laboratory experiment has a scale of 1:10000 for distance and 10000:1 for frequency. Our model with horizontal and vertical lengths of 450 mm and 150 mm corresponds to 4500 m and 1500 m for a real-world seismic survey. The transducers produce dominant frequencies of 500 kHz that scales down to 50 Hz. The physical model consists in a water layer over a PVC slab that overlies another water layer, which in turn overlies a PLX slab with a cut channel (figure 2). In the experiment, we simulate two wells, B and C, that will be used as a blind well and for calibrating the gradient, respectively.

Fifty shots were recorded over a distance of 2500 m. The source and receiver intervals are 50 and 10 m, respectively. Each shot was recorded with a 1000-m-offset symmetrical spread. An example of a seismic shot is shown in figure 3. The source and receivers were located inside the water tank at a depth of approximately 250 m, and the PVC is located 500 m below the source-receiver datum. In this way, the see-bottom multiple arrives at a time of 1.69 seconds and does not interfere with the reflections of interest, which are above 1.4
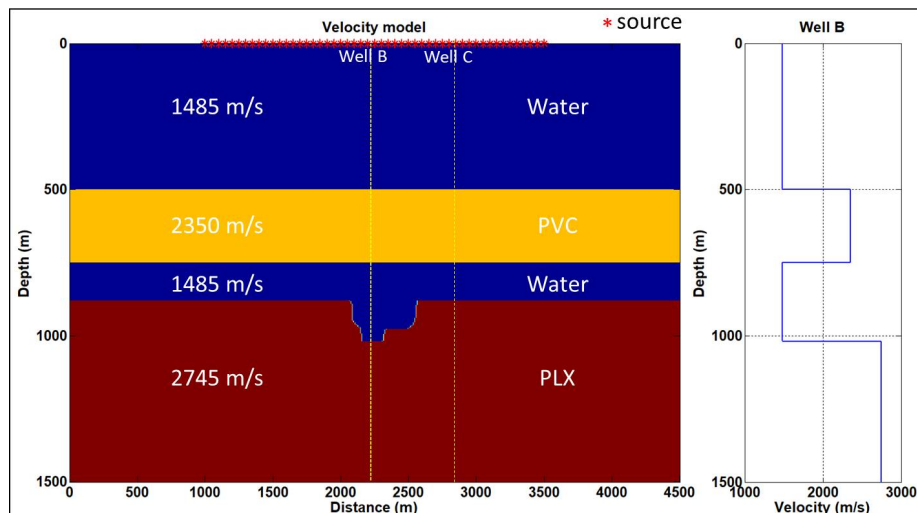
FIG. 2. Velocity model used to generate physical modelling shots.

seconds. The main events are: direct arrival, the primary reflections of water-PVC, PVC-water and water-PLX interfaces, as well as multiples A, B and C. The acrylic slab is actually conformed by two slabs. They are not perfectly welded and produce a weak reflection at a time around 1.55 seconds. We obtained a stack velocity model by applying velocity
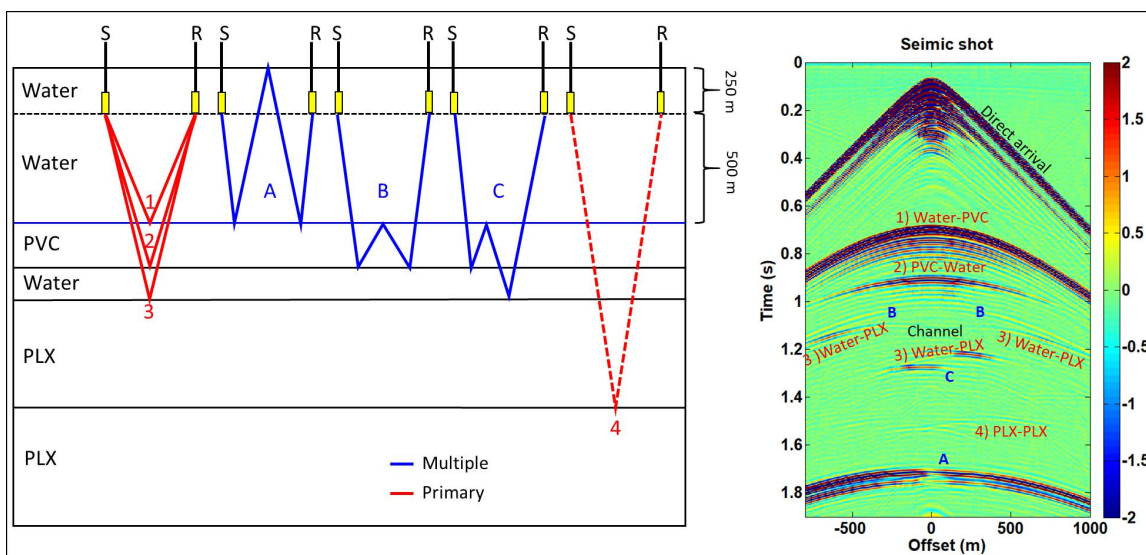

FIG. 3. Example of a seismic shot from physical modelling. Seven main events were identified.

analysis to several CMP gathers. An example of the picking-velocity process is shown in figure 4. The first panel shows the velocity semblance and the numbers correspond to the events shown in figure 3. The direct arrival was muted before the velocity analysis. The second panel displays the NMO-corrected gather by using the velocities picked in panel 1. The stacked trace is plotted in panel 3. The stack and interval velocities are displayed in panels 4 and 5, respectively. The interval velocity (blue curve) was obtained by applying Dix's equation and is compared to the interval velocity (red curve) that comes from the

well.

The stack section is shown in figure 5. We can identify all the seismic events shown in figure 3. We used the stack velocity model to obtain an interval velocity model which was smoothed in order to be the input for the first iteration of the inversion process. We will use a maximum time of 1.4 seconds for the inversion.
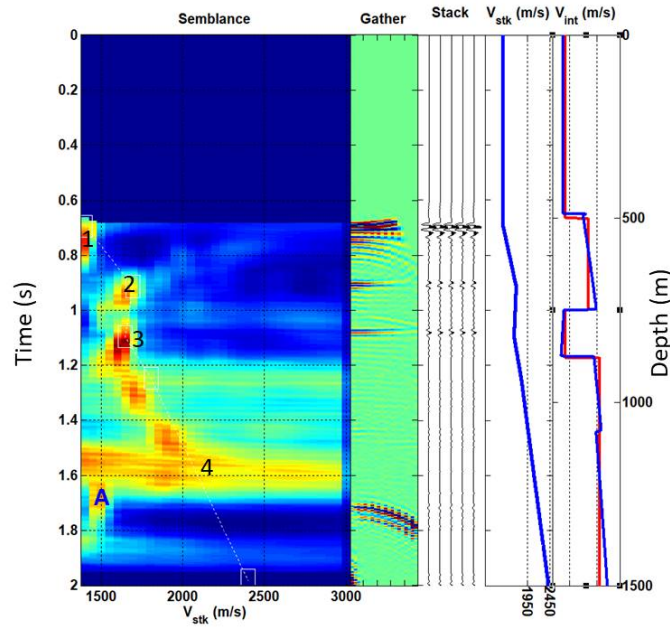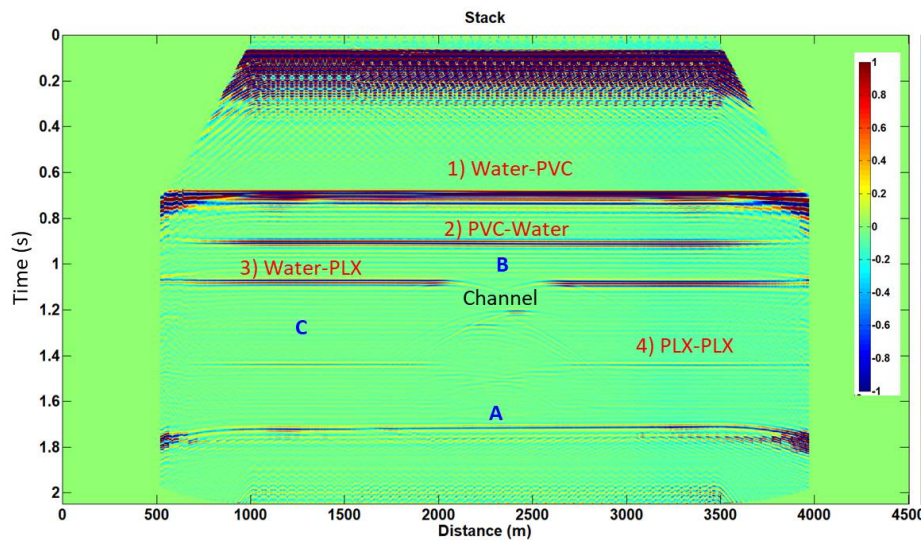

FIG. 4. Velocity analysis.

FIG. 5. Stack section.

DATA CONDITIONING

The processes applied to the data can be separated into two groups. The first group has the purpose of making the laboratory data more similar to real seismic data. These processes correct the source-receiver directivity and the changing waveform with offset effects (Buddensiek et al., 2009). The second group addresses geometrical spreading and low frequency noise.

Source-receiver directivity correction

Directivity of a source or sensor refers to whether it is omni-directional or more sensitive in some directions (Lemon, 1981). Piezoelectric transducers do not radiate as point sources or receive as point sensors. They have a pronounced directional response caused by wave interference effects that affect the amplitude-with-offset behavior of the recorded seismic shot. Mahmoudian et al. (2012) analyzed the amplitude variation with angle and azimuth of physical modelling data and derived anisotropy parameters. The authors highlight the importance of correcting the data for directivity when the experiment requires to analogize the amplitude of physical modelling data to real seismic data.

Equations 3 and 4 describe the directivity response for circular transducers (Krautkrämer and Krautkrämer, 1986) . A derivation of these equations can be found in Wong and Mahmoudian (2011).

$$A = 4A_o \frac{J_1(X)}{X} sin(\frac{\pi D}{8\lambda z}) \tag{3}$$

$$X = \frac{\pi D}{\lambda} sin\gamma \tag{4}$$

$$J_1(x) = \frac{x}{2} - \frac{x^3}{2^2 4} + \frac{x^5}{2^2 4^2 6} - \frac{x^7}{2^2 4^2 6^2 8}... \tag{5}$$

where A_o is initial amplitude or pressure field, D is effective diameter of the piezoelectric crystal, λ is wavelength, z is the distance from the emitting plane to a reference plane, γ is the angle to the vertical axis, and J_1 is the Bessel function of order 1 (Equation 5). A schematic representation of the transducer and the variables needed to calculate the radiation patterns is shown in figure 6.

The transducers used in this experiment have a disc shape with diameters on 1.3 mm (13 m in real-world scale), and are operated at a dominant frequency of 500 kHz (50 Hz in real-world scale). The wavelength in the water layer is 30 m considering a velocity of 1500 m/s and the dominant frequency of 50 Hz. The directivity patterns for transducers with these characteristics is shown in figure 7-A. We also show an example of the directivity pattern for a dominant frequency of 150 Hz (figure 7-B). In this case the effect is more pronounced and a larger correction would be needed.
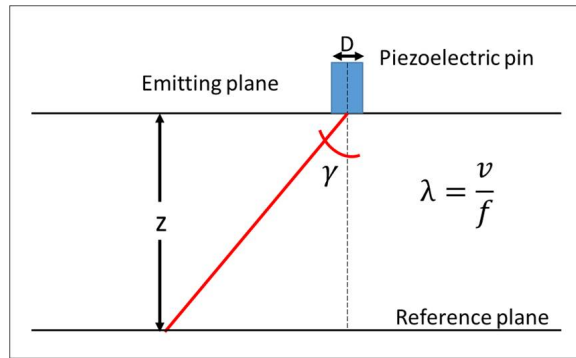
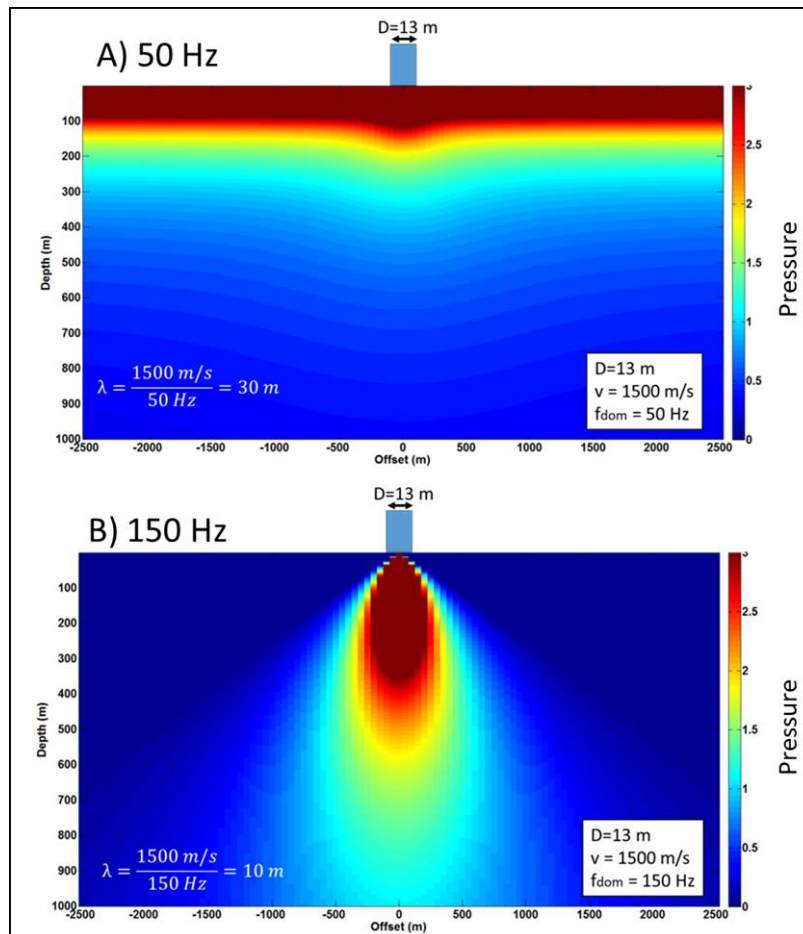FIG. 6. Variables needed to calculate radiation patterns of a disc transducer.

FIG. 7. Comparison between radiation patterns with $A) f_{dom} = 50$ Hz and $B) f_{dom} = 150$ Hz. The scaled transducer diameter is 13 m. The velocity is 1500 m/s.

We are interested in the pressure along the first interface (the PVC slab at a depth of 500 m) which is shown by the profile of figure 8. The inverse of this curve represents the amplitude correction that will be applied to reflections from the water-PVC interface. The correction for deeper reflections depends on the first interface correction. We used ray tracing to obtain the directivity correction for deeper times. Figure 9 shows a three-layer

medium and the radiation pattern produced by transducer /(S) over the first layer. Red and orange rays correspond to reflections from the first and second interfaces, respectively. The correction for the red events will be calculated at the position of the reflections (on the red points). The correction for the second reflector is calculated in the transmission points (in orange).
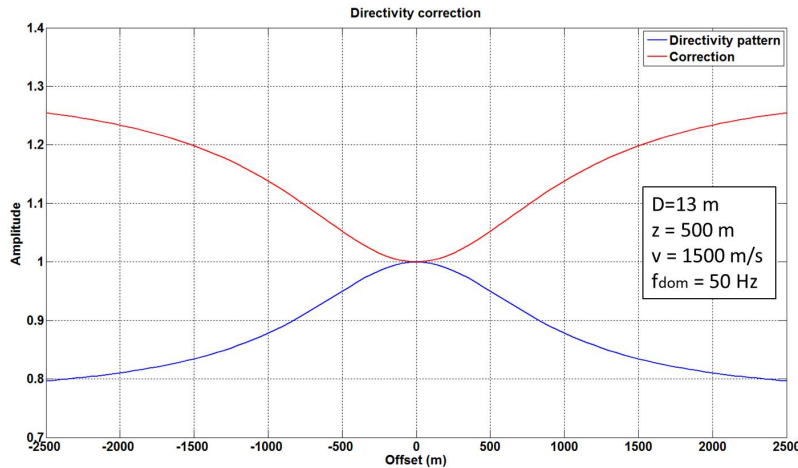

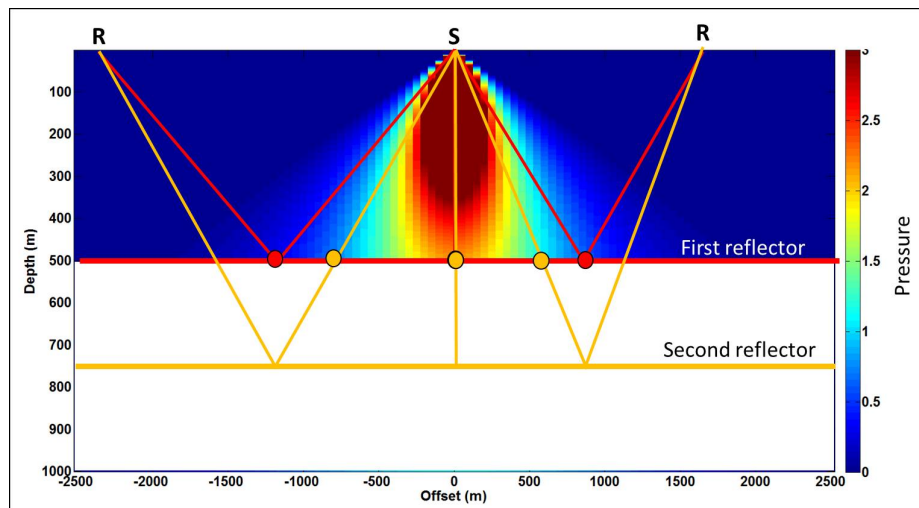FIG. 8. Directivity pattern (blue) and correction (red) for a interface at a depth of 500 m.

FIG. 9. The directivity correction for the first and second reflectors are taken from the location of the red and orange points respectively. S is the source transducer. R is the receiver transducer.

The corrections are calculated by taking as references depth and offset; however, they will be applied to seismic shots, which are in time. We can transform from depth to time by using the information from ray tracing. Once we have the corrections in time, they are interpolated between interfaces and extrapolated from the first layer to the surface and from the last layer to the bottom. The final correction is a matrix in time and offset domains that can be applied directly to the shots by multiplication (figure 10).
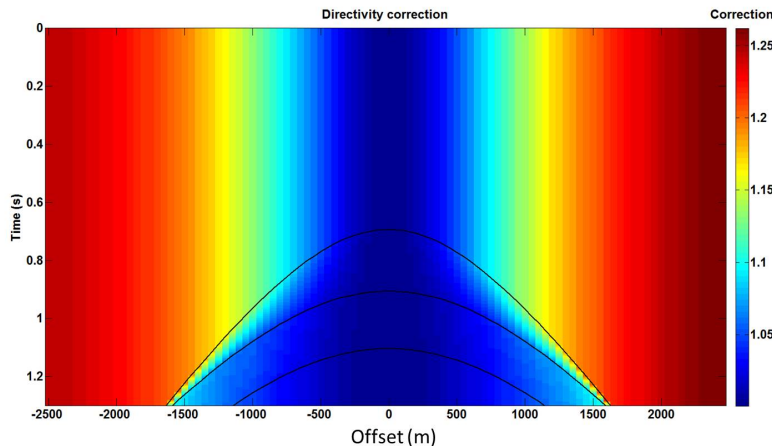
FIG. 10. Directivity correction in time and offset domains.

Changing-waveform correction

A transducer doesn't work as an isolated point source, but as an array of point sources. Each point at the disc surface has to be considered a source. The same applies to receiver transducers. The seismic record is the sum N^2 traces, where N is the number of points on the disk. When the diameter is the same size as or larger than the emitted wavelength, interference among traces will result in a waveform change. Figure 11 illustrates this phenomenon for the hypothetical case of a 3-point transducer. The final trace would be the sum of 9 traces with different arrival times. The main impact will be a loss of high frequencies and a decrease in amplitude.

In order to observe the changing-waveform effect and propose a correction, we simulated the phenomenon by generating traces for all source and receiver points. We used a scaled point size of 1 m for this experiment. The process of generating traces works as follows: we used a two-layer model and calculated the travel time for each source-receiver point; we located a spike in the respective travel time and convolved with a 50-Hz dominant frequency Ricker wavelet. These traces are then summed up and divided by the number of points in order to simulate a hypothetical trace that would be recorded in the source-receiver transducer system. We also created another trace simulating single point transducers. This trace will be taken as reference to evaluate the changing-waveform issue. The comparison between the amplitude of these two traces will provide the correction. We assumed that the wavelet is stationary in this process.

Figure 12 compares the changing-waveform effect for two different dominant frequencies, 50 and 150 Hz. The velocity of the water layer is 1500 m/s, so that the wavelengths are 30 and 10 meters, respectively. The scaled diameter of the transducer is 13 m. We are plotting the reference trace in blue and the transducer trace in red for offset from zero to 1000 m. We observe a subtle loss of high frequencies and an amplitude decrement as we go to larger offsets for the 50-Hz case, which is the case of our laboratory experiment. For the 150-Hz case, the waveform drastically changes with offset, the amplitude spectrum is moved to the low frequencies, while high frequencies are lost.

We conclude that the wavelet phase doesn't change significantly for a transducer diameter of 13 m and wavelengths greater than 30 m. Therefore, we just considered an amplitude correction that can be derived by comparing the maximum amplitude of the reference to transducer wavelets. This procedure was done for the three reflectors that constitute our physical model. The amplitude correction curves are shown in figure 13. These corrections are already in time and offset domains, we just need to interpolate between curves and extrapolate from the first interface to the surface and from the last interface to the bottom to obtain a matrix that corrects the shot by the waveform-changing effect. This matrix is similar to the one shown in figure 10.
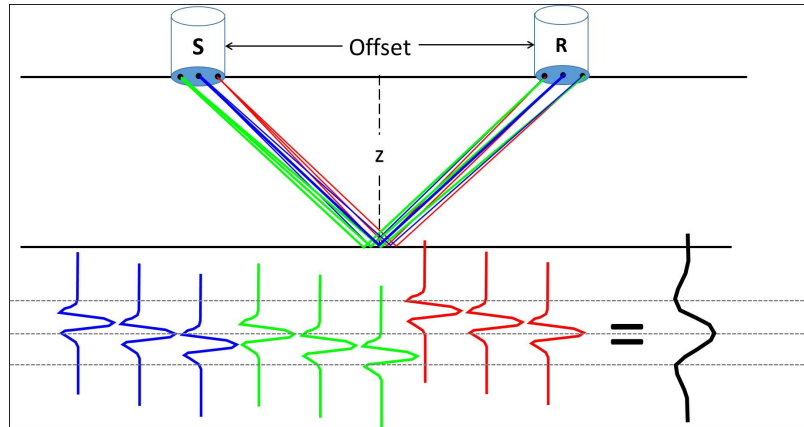

FIG. 11. Mechanism that changes the waveform with offset when relatively small wavelengths propagate between two spatial transducers of diameter D. Each color corresponds to the contribution of a source point.
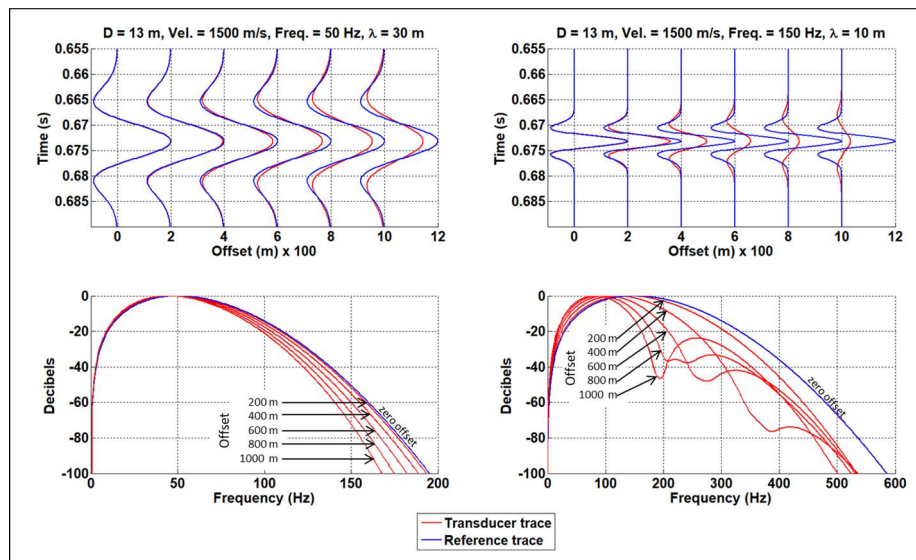

FIG. 12. Waveform-change effect for 50 and 150 Hz-dominant frequencies. Velocity is 1500 m/s, scaled transducer's diameter is 13 m.
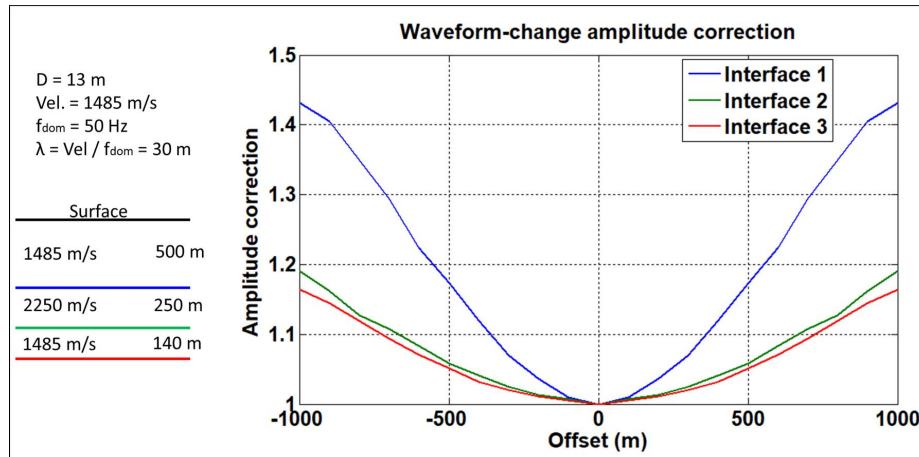
FIG. 13. Waveform-change correction for a scaled transducer diameter of 13 m and wavelength of 30 m.

From 3D to 2D geometrical spreading

The forward finite difference modelling that we used in the inversion process assumes a two-dimensional model. This implies that the synthetic amplitudes spread in 2D and decay with the square root of distance. However, amplitudes generated by point sources in a 3D world decay with the inverse of distance, approximately. Therefore, we must apply a geometrical spreading correction that takes the data from 3D to 2D. We applied an approximate correction based on the time-domain asymptotic solution given by Bleistein (1984). The correction consists in a multiplication of each time domain trace by the function $\sqrt{t}$ on a sample by sample basis to correct amplitudes, followed by a time-domain convolution with the function $\frac{1}{\sqrt{t}}$ to adjust phases. This is a common approach where 2D-FWI inversion is applied to real or physical modelling data (Pratt, 1999). Auer et al. (2013) discussed the validity of this 3D-to-2D transformation in the context of crosshole seismic full-waveform tomography.

Figure 14 shows the result of applying the 3D-to-2D geometrical spreading correction. Traces in the real 3D world (blue) lose amplitude faster than traces in a 2D world (red).

Low frequency picks

The amplitude spectrum of the shots confirms that the dominant frequency is 50 Hz (figure 15). If we zoom in the frequency band between 0 and 20 Hz, we observe that there are picks of low frequency that can potentially damage the inversion (figure 16-A). We applied a high-pass band filter to remove these frequency picks before the inversion (figure 16-B).

Wavelet estimation

The wavelet estimation was done in four steps. The first step consists in estimating a minimum phase wavelet that matches the amplitude spectrum of the seismic shot at the
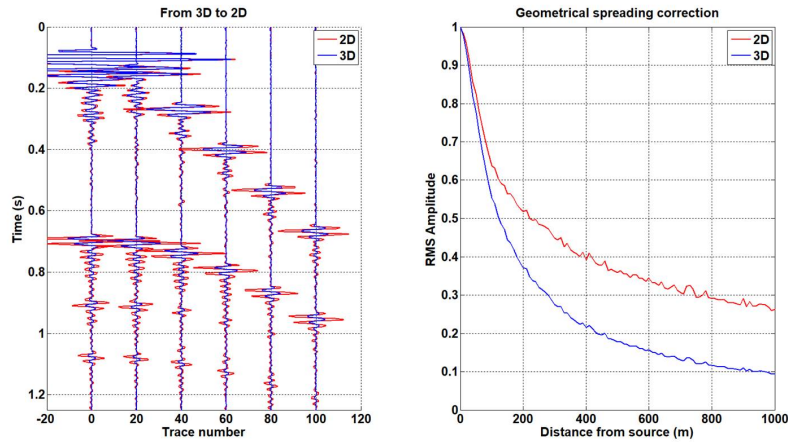
FIG. 14. From 3D to 2D geometrical spreading. Blue traces are the original ones. Red traces emulate 2D geometrical spreading.
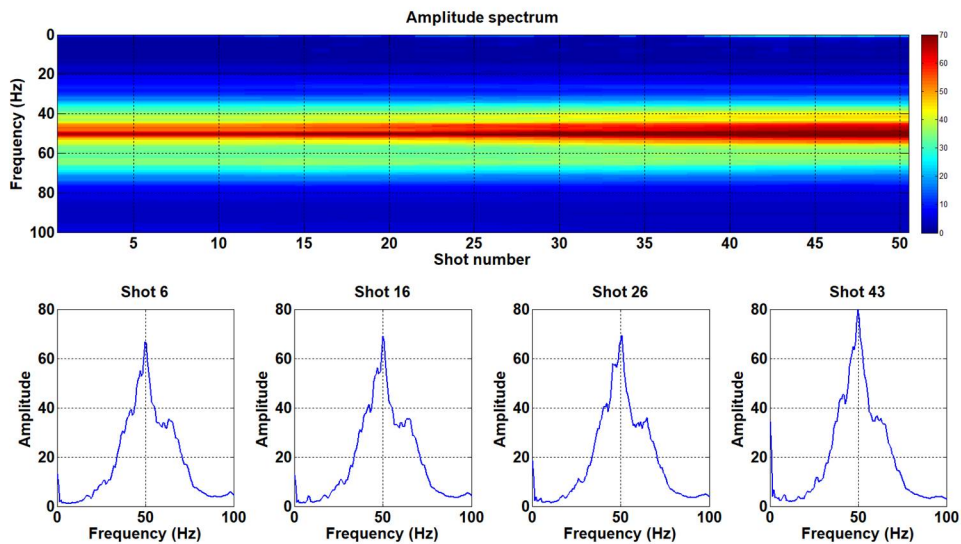

FIG. 15. Amplitude spectra of all shots.

well location. This was done by using "waveletestimator" from CREWES-MATLAB tool box (figure 17). A review of this program can be found in Lloyd and Margrave (2012). In the second step, we constructed a horizontal-layer model using well-velocity information. Then we generated a shot with the estimated wavelet over this model by using the acoustic forward modelling that we will later apply for the inversion. The third step consists in comparing the zero offset traces of the synthetic and real shots. From this comparison we obtained a matched filter that produces the best fit between real and modelled traces. Finally, this matched filter is applied to the estimated wavelet in order to produce a calibrated one that will be used for generating synthetic shots in the process of FWI. Figure 18 shows the comparison between real and synthetic traces. They have an acceptable match from 0.6 to 1 seconds; however, the third seismic event, between 1.2 and 1.3 seconds, seems to be attenuated if compared to the synthetic event which does not model attenuations effects.
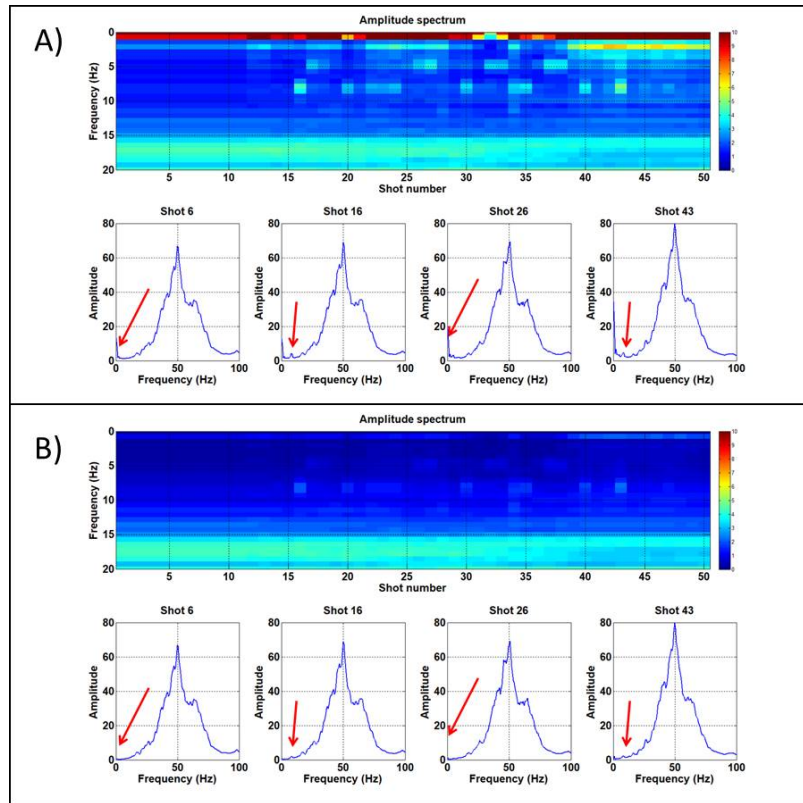
FIG. 16. A zoom in the low frequency band shows picks of low frequency noise (A) that were removed by applying a high-pass filter (B).

In order to partially compensate this issue, we will use a non-stationary matched filter to calibrate the gradient.

INVERSION METHODOLOGY

We used monoparameter-FWI methodology to derive P-wave velocity from physical modelling seismic data. The four steps of the FWI cycle are:

1) Generating synthetic seismic data (modelled shots) from a smoothed initial model and calculation of the data residual (difference among observed and modelled shots).

The synthetic shots are produced with a finite-difference acoustic algorithm with constant density. The initial velocity model is a smoothed version of the interval velocities derived from the stack velocities (figure 19-A). The modelled shots for this iteration are constituted mainly by the direct arrival. There isn't any reflection because the smoothed initial model doesn't have any significant velocity contrast (figure 19-B). The data residual will be mainly the original shot with subtle changes in the low frequencies. The direct wave in the observed shots has a strong ringing character specially for the short offset traces. For this reason we muted this event in the data residuals before the next step.

2) Pre-stack depth migration of the data residual (using the current velocity model) and stack.
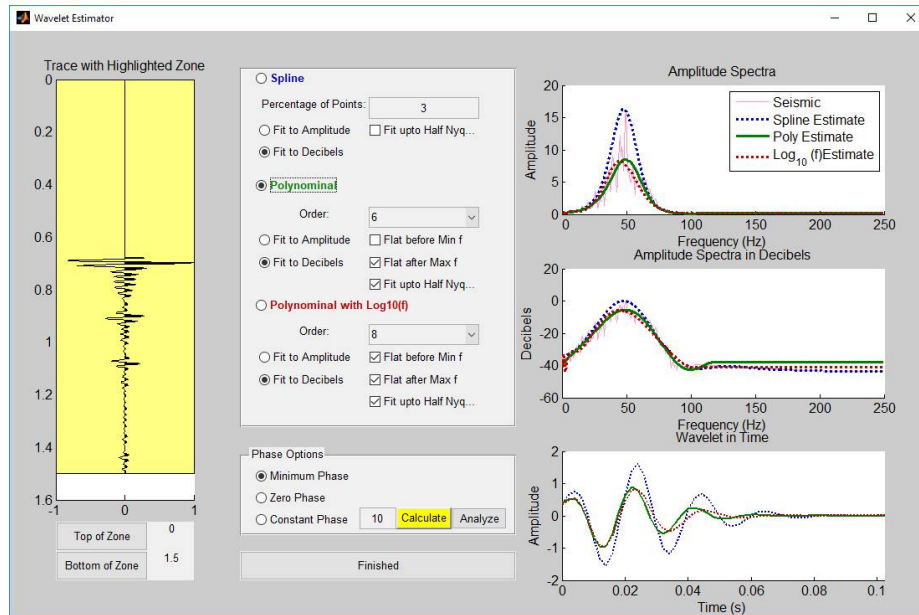
FIG. 17. Main screen of "waveletestimator" program. The options Polinomial of 6, flat after maximum frequency and fit upto half Nyquist were chosen after several tests.
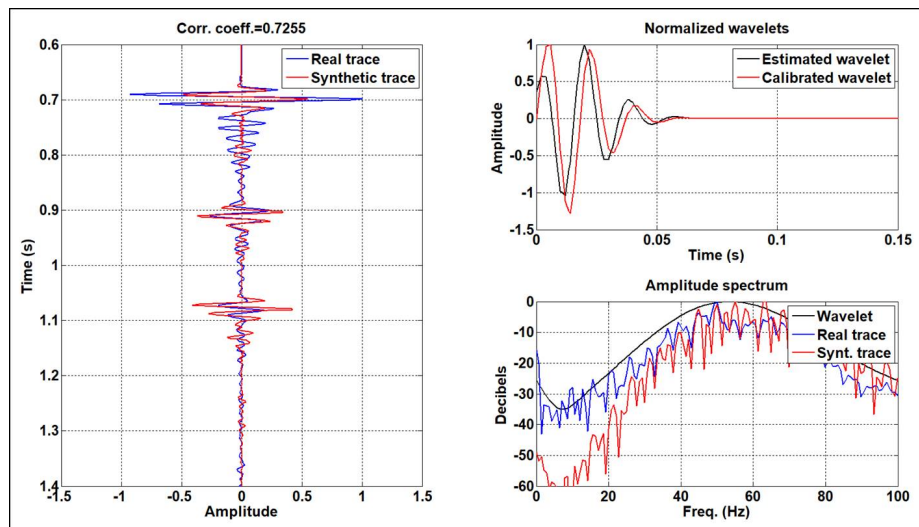

FIG. 18. Matching finite-difference-modelled and real traces in order to obtain a calibrated wavelet which will be used in the inversion.

This step builds the gradient. Following IMMI's perspective, we used PSPI migration with a deconvolution imaging condition, which works as a gain correction. This is similar to the role of the main diagonal elements of the inverse Hessian (Shin et al., 2001). Margrave et al. (2010) described two procedures to produce the gradient: one option is a frequency multi-scale approach, where we start the inversion with low frequencies and introduce higher frequencies as we iterate. PSPI is very convenient for this case because it allows selecting the frequency range that we want to migrate. The second procedure consists in migrating the whole frequency band and applying a wide Gaussian smoother for the first iteration, allowing the pass of long wavelengths. As we iterate, the half-width
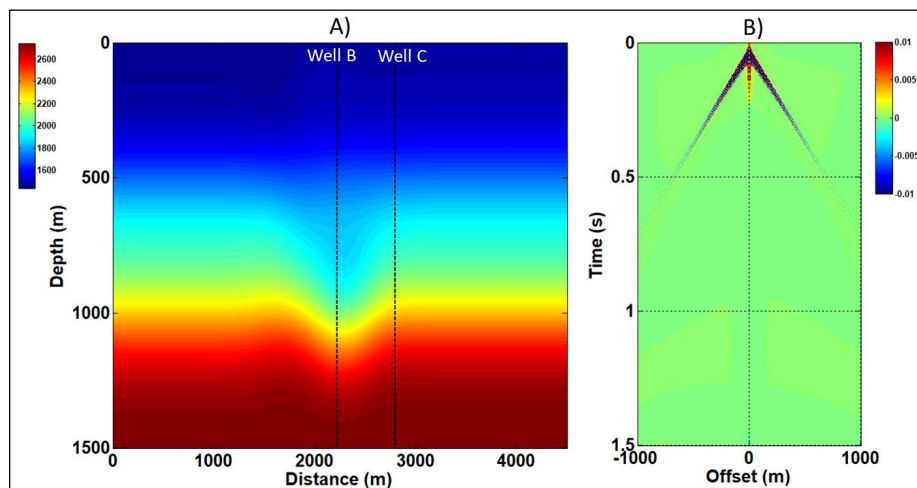
FIG. 19. A) Initial velocity model. B) Synthetic shot modelled by finite differences through the initial velocity model.

size of the Gaussian smoother is reduced, allowing the pass of shorter wavelengths. This can be considered a space multi-scale approach. As we mentioned before, the seismic data have a dominant frequency of 50 Hz, and the model that we want to solve has a dominant frequency of around 5 Hz. These characteristics of the problem restrict the scope of the frequency multi-scale approach. For this reason, we choose the Gaussian smoother strategy, which showed great potential to recover low frequency information. Under this approach, the gradient was obtained by migrating frequencies from 0 to 80 Hz and then prioritizing a wide smoother with half-width of 160 m for the first iteration. We designed a strategy for the Gaussian smoother that allows to incorporate the influence of more than one half-width window. This strategy is explained in detail in the next section.

3) Scaling or calibrating the gradient by using well-log velocity.

This step produces a velocity update. The well calibration technique was described by Margrave et al. (2010). We want to find a scalar λ such that Equation 6 is minimized.

$$\int (v_{true}(x_w, z) - v_k(x_w, z))^2 dz \qquad (6)$$

where x_w is the well location at which v_{true} is known, v_k is taken from current velocity at the well location.

The procedure goes as follows: firstly, the difference δvel between true and model velocities is calculated in the calibration well location. The second step consists in estimating an amplitude scalar a and a phase rotation ϕ that make the gradient trace g more like δvel. The scalar a is found such that $\delta vel - ag$ is minimized by least squares. Finally, a convolution matched filter is obtained with a and ϕ.

When we previously showed the estimation and calibration of the wavelet, we conjec-

tured that attenuation may be affecting physical modelling data, which prevents us from obtaining a better update. In order to address this issue, we used a non-stationary matched filter that is expected to compensate amplitude losses with depth (Romahn and Innanen, 2017). The procedure to obtain a depth-varying matched filter is similar to the methodology described above. However, this time we are using a window to calculate a matched filter per each depth sample, instead of using the whole well interval. A size window of 600 m produces good results. Finally, we construct a convolution matrix by locating each filter at its respective depth. The multiplication of this matrix by each gradient trace will produce the velocity update. Figure 20 compares the velocity updates obtained with stationary and depth-varying filters. The second case helps to recover information from deeper parts of the model, which suggests that it is helping to diminish the attenuation issue.
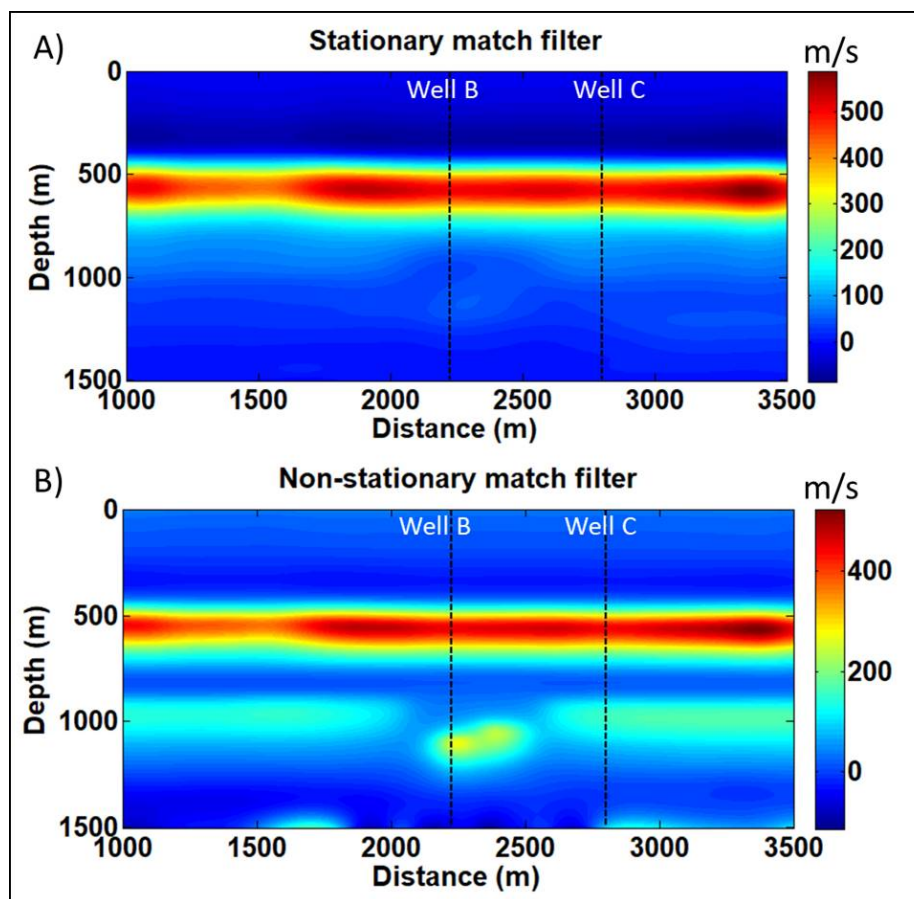

FIG. 20. A) Velocity update produced with a stationary matched filter and B) velocity update produced with a non-stationary matched filter for the first iteration.

4) The sum of the current velocity model and the update provides a new velocity model that will be used in the next iteration (figure 21).

Gaussian smoother strategy

The Gaussian smoother works as a high-pass wavelength filter. The half-width window has the function of establishing the cutoff wavelength. Figure 22 shows the spatial Fourier
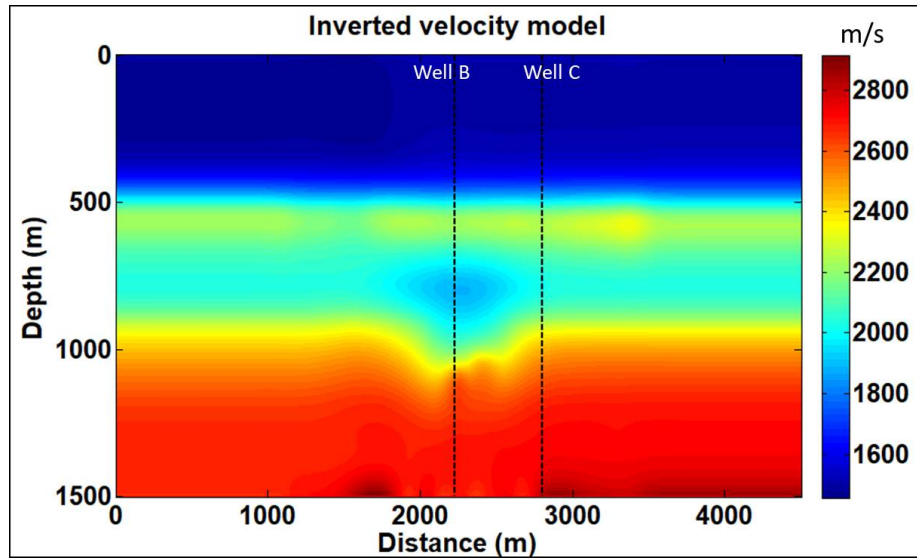
FIG. 21. Inverted velocity model for iteration 1. It is the result of adding the velocity update to the initial model.

transform of a Gaussian smoothers with half-width window of 160 m. This smoother starts to attenuate wavelength smaller than 320 m and cut wavelengths smaller than 160 m. The relevant wavelengths to reconstruct the true model are greater than 300 m, considering the smaller velocity (1500 m/s) and the frequency model of 5 Hz. For this reason, we repeatedly used this half-width window in the first 10 iterations, expecting to recover wavelengths grater than 300 meters as much as possible.
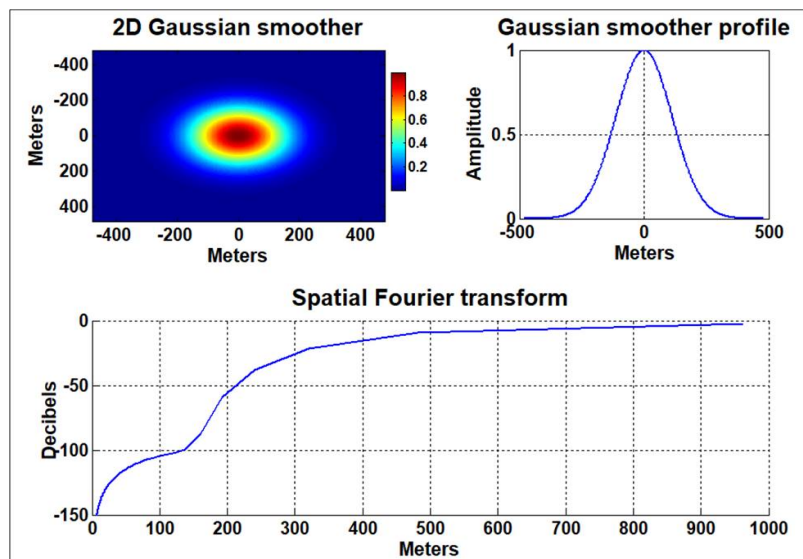

FIG. 22. Gaussian smoother with a half-width window of 120 m. Its spatial Fourier transform shows the filtered wavelengths.

We adapted the Gaussian smoother approach in order to allow the influence of several half-width windows while emphasizing on one of them in each iteration. In order to do so, we obtained, in each iteration, a set of gradients smoothed with a different half-window

from 10 to 160 m. Then we scaled each gradient by applying the well calibration technique which produces a set of preliminary velocity updates (figure 23). We want to use all the preliminary velocity updates while giving priority to, for example, the update with the half-width window of 100 m. For this purpose, we use a probabilistic function where each of its elements correspond to each half-window, the values of the function add one, and the greater value corresponds to the smoother that we want to emphasize (figure 24). The probabilistic function works as a weight function. We obtained a final velocity update by multiplying the probabilistic function to the set of preliminary updates and then adding them. The half-width windows that we emphasized in each iteration are shown in Table 1. Figure 25 shows the comparison between a velocity update obtained by using a conventional Gaussian smoother with half-width of 160, and the update obtained by applying the strategy described above. The adapted Gaussian smoother provides an improved and more focused update.
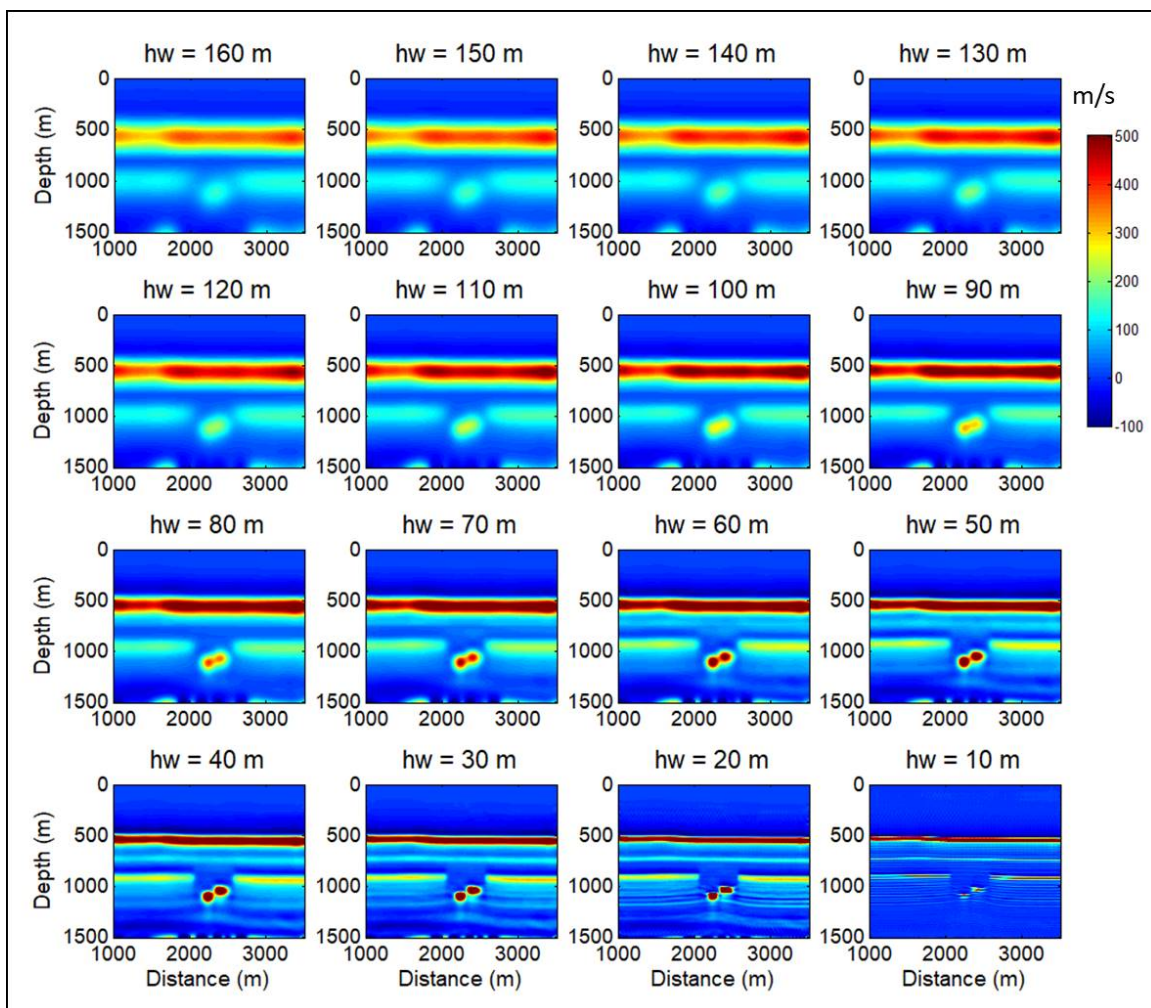

FIG. 23. Preliminary velocity updates obtained from a gradient smoothed with several half-width windows for the first iteration.
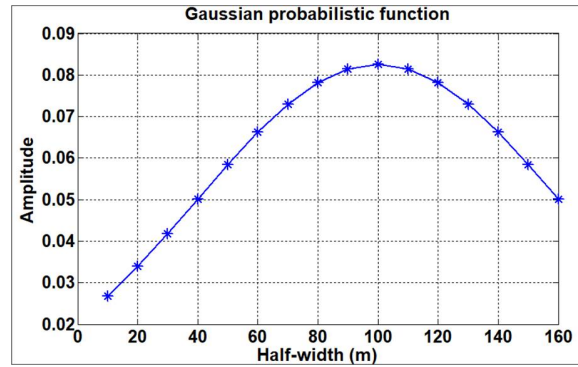
FIG. 24. Gaussian probabilistic function. The sum of the elements is one. When multiplied to the preliminary updates works as a weight function.
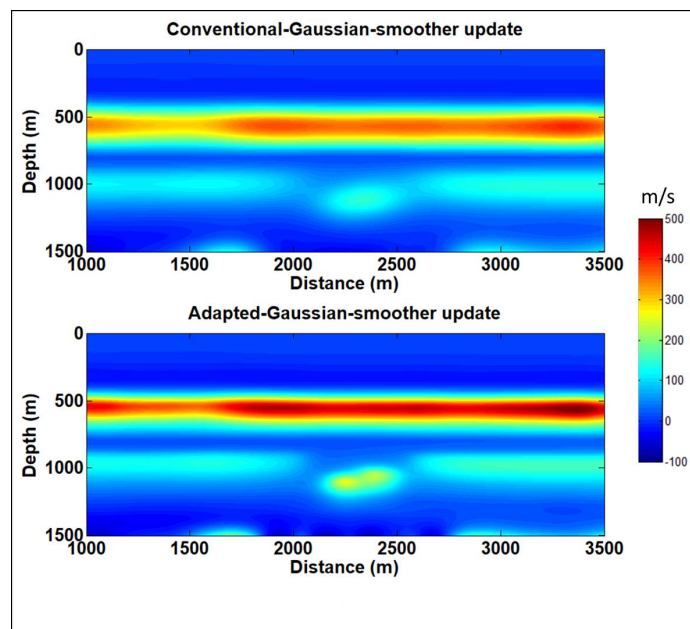

FIG. 25. Conventional-Gaussian-smoother update vs adapted-Gaussian-smoother update for a half-width of 160 m and first iteration.

RESULTS

Figure 26 shows the inverted velocity model and its comparison to the initial and true models. The inversion is able to recover the four layers of the true model. The location and shape of the channel are well defined; however, the velocity inside the channel is being overestimated. The interfaces water-PVC and PVC-water are better constructed, but we couldn't define the edges of the layers.

Figure 27 shows the velocity error with iteration in model and in the locations of blind and calibration wells. We observe that the error in the calibration well always decreases with iteration because the matched filter was designed with that purpose. The error in the blind well also steadily decreases with each iteration, but in a smaller rate.

Table 1. Half-width used in each iteration

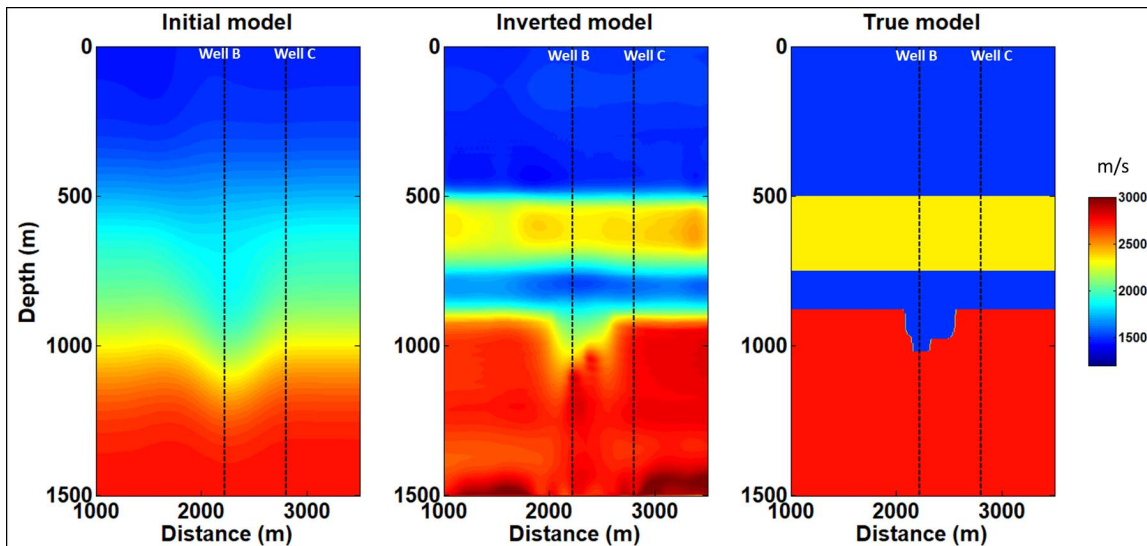| Iteration	1-10	11-20	21-25	26-30
Half-width (m)	160	100	40	20

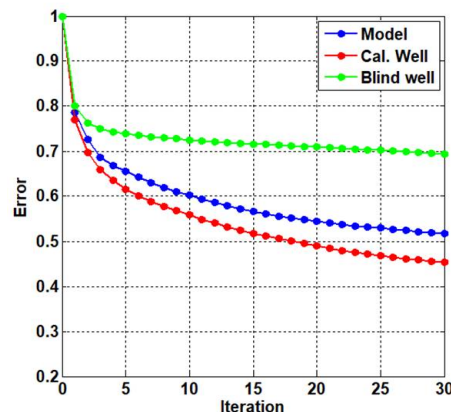FIG. 26. Initial, inverted and true velocity models.

FIG. 27. Error in blind well B, calibration well C and in the whole model.

Figure 28 shows the comparison between an observed shot and a final-modelled shot. The L2Norm suggests a convergence from the fith to the 30th iteration. The modelled shot resembles the characteristics of the true shot. However, there are significant differences in amplitude and phase. There are several factors that may be producing this effect: 1) The final inverted model was not able to recover the interface edges, which causes a smaller amplitude in the modelled shot. 2) The estimated wavelet is far to be optimal. 3) The physics assumptions of the forward modelling does not fit the complex wave propagation phenomenon of the true shots. Notwithstanding all these factors, the strategy applied in this

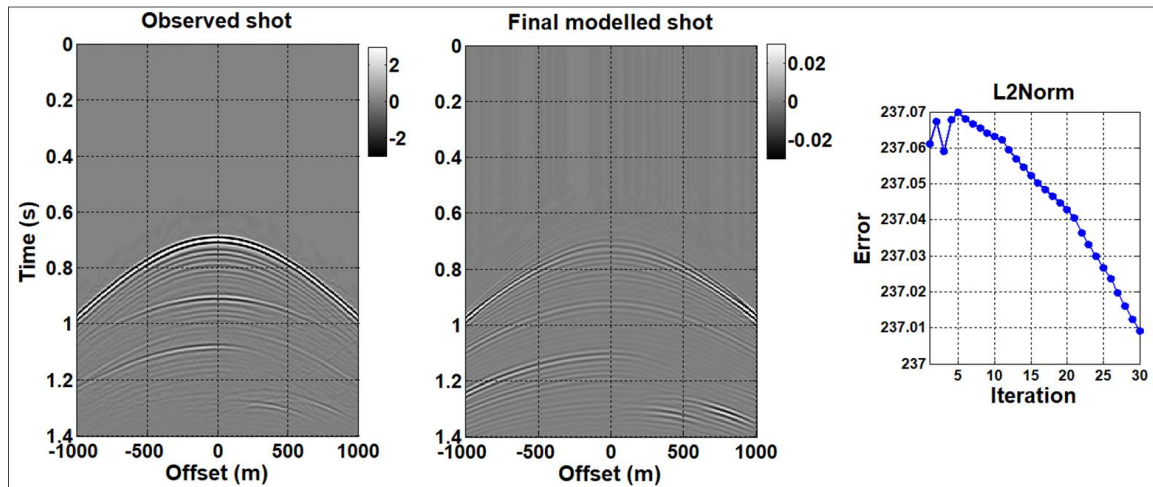work showed great potential in the recovery of long-wavelength information from reflection seismic data.

FIG. 28. Comparison between true and final modelled shot.

CONCLUSIONS

CREWES seismic physical modelling laboratory facility is a valuable tool for appraising new seismic processing and interpretation techniques outside the controlled synthetic environment. The challenge of using this kind of data is that they have to be conditioned in order to be treated as real seismic data. We evaluated a nonstandard FWI approach that is referred as iterative modelling, migration and inversion. Examples of the flexibility of this type of inversion in our experiment are: 1) The use of PSPI migration to obtain the gradient. 2) Derivation of non-stationary matched filters from well-log velocity to calibrate the gradient. 3) Iterative application of Gaussian smoothers to frequency-band fixed migrated data residuals as an alternative to the frequency multi-scale technique.

The characteristics of the physical model (dominant frequency around 5 Hz) and the observed shots (dominant frequency of 50 Hz) constitute an enormous challenge in our experiment, because we are using PSPI migration to obtain the gradient. PSPI uses one-wave operators to migrate the seismic data. This property limits its capacity to recover long wavelengths. The strategy of using non-stationary matched filter to calibrate the gradient (instead of the step length method) and iteratively applying Gaussian smoothers to the gradient (instead of frequency multi-scale approach), showed great potential to recover long-wavelength information from reflection seismic data.

ACKNOWLEDGEMENTS

REFERENCES

Auer, L., Nuber, A. M., Greenhalgh, S. A., Maurer, H., and Marelli, S., 2013, A critical appraisal of asymptotic 3d-to-2d data transformation in full-waveform seismic crosshole tomography: Geophysics, **78**, No. 6, R235–R247.

Bleistein, N., 1984, Two-and-one-half dimensional in-plane wave propagation: Geophysical Prospecting, **34**, 686–703.

Buddensiek, M. L., Krawczyk, M., Kukowski, N., and Oncken, O., 2009, Performance of piezoelectric transduces in terms of amplitude and waveform: Geophysics, **74**, No. 2.

Cai, J., and Zhang, J., 2015, Acoustic full waveform inversion with physical model data: 2015 Workshop: Depth Model Building: Full-waveform Inversion, Beijing, China, 146–149.

Krautkrämer, J., and Krautkrämer, H., 1986, Werkstoffprüfung mit ultraschall.

Lailly, P., 1983, The seismic inverse problem as a sequence of before stack migration: SIAM, 206–220.

Lemon, D. K., 1981, A review of advanced acoustic emission sensors (no. 23111-04210): PACIFIC NORTH-WEST LABS RICHLAND WA.

Lloyd, H. J. E., and Margrave, G. F., 2012, Well tying and trace balancing hussar data using new matlab tools: CREWES Research Report, **24**.

Mahmoudian, F., Wong, J., and Margrave, G. F., 2012, Azimuthal avo over a simulated fractured medium: A physical modeling experiment, *in* SEG Technical Program Expanded Abstracts 2012, Society of Exploration Geophysicists, 1–5.

Margrave, G. F., Fergurson, R. J., and Hogan, C. M., 2010, Full-waveform inversion with wave equation migration and well control: CREWES Research Report, **22**.

Margrave, G. F., Innanen, K. A., and Yedlin, M., 2012, A perspective on full-waveform inversionl: CREWES Research Report, **24**.

Pratt, R. G., 1999, Seismic waveform inversion in the frequency domain, part 1: Theory and verification in a physical scale model: Geophysics, **64**, No. 3, 888–901.

Romahn, S., and Innanen, K. A., 2017, Iterative modeling, migration, and inversion: Evaluating the well-calibration technique to scale the gradient in the full waveform inversion process: SEG Technical Program Expanded Abstracts 2017, 1583–1587.

Shin, C., Yoon, K., Marfurt, K. J., Park, K., Yang, D., Lim, H. Y., Chung, S., and Shin, S., 2001, Efficient calculation of a partial-derivative wavefield using reciprocity for seismic imaging and inversion: Geophysics, **66**, No. 6, 1856–1863.

Tarantola, A., 1984, Inversion of seismic reflection data in the acoustic approximation: Geophysics, **49**, 1259–1266.

Virieux, A., and Operto, S., 2009, An overview of full-waveform inversion in exploration geophysics: Geophysics, **74**, 1259–1266.

Wong, J., Hall, K., Gallant, E., Maier, R., and Bertram, M., 2009, Seismic physical modeling at the university of calgaryl: CSEG Recorder, **36**, 25–32.

Wong, J., and Mahmoudian, F., 2011, Physical modeling ii: directivity patterns of disc transducers: CSEG Recorder, **23**.